



# Production of nanoparticles during experimental deformation of smectite and implications for seismic slip

S. Aretusini<sup>a,\*</sup>, S. Mittempergher<sup>b</sup>, O. Plümper<sup>c</sup>, E. Spagnuolo<sup>d</sup>, A.F. Gualtieri<sup>e</sup>,  
G. Di Toro<sup>a,d,f</sup>

<sup>a</sup> School of Earth and Environmental Sciences, University of Manchester, Manchester, UK

<sup>b</sup> Dipartimento di Scienze della Terra, Università degli Studi di Torino, Torino, Italy

<sup>c</sup> Department of Earth Sciences, Utrecht University, Utrecht, The Netherlands

<sup>d</sup> Sezione di Tettonofisica e Sismologia, Istituto Nazionale di Geofisica e Vulcanologia, Roma, Italy

<sup>e</sup> Dipartimento di Scienze Chimiche e Geologiche, Università degli Studi di Modena e Reggio Emilia, Modena, Italy

<sup>f</sup> Dipartimento di Geoscienze, Università degli Studi di Padova, Padova, Italy

## ARTICLE INFO

### Article history:

Received 15 September 2016

Received in revised form 30 January 2017

Accepted 31 January 2017

Editor: J. Brodholt

### Keywords:

smectite

earthquakes

friction

nanoparticles

clay amorphization

## ABSTRACT

Nanoparticles and amorphous materials are common constituents of the shallow sections of active faults. Understanding the conditions at which nanoparticles are produced and their effects on friction can further improve our understanding of fault mechanics and earthquake energy budgets. Here we present the results of 59 rotary shear experiments conducted at room humidity conditions on gouge consisting of mixtures of smectite (Ca-montmorillonite) and quartz. Experiments with 60, 50, 25, 0 wt.% Ca-montmorillonite, were performed to investigate the influence of variable clay content on nanoparticle production and their influence on frictional processes. All experiments were performed at a normal stress of 5 MPa, slip rate of  $0.0003 \leq V \leq 1.5 \text{ ms}^{-1}$ , and at a displacement of 3 m. To monitor the development of fabric and the mineralogical changes during the experiments, we investigated the deformed gouges using scanning and transmission electron microscopy combined with X-ray powder diffraction quantitative phase analysis. This integrated analytical approach reveals that, at all slip rates and compositions, the nanoparticles (grain size of 10–50 nm) are partly amorphous and result from cataclasis, wear and mechanical solid-state amorphization of smectite. The maximum production of amorphous nanoparticle occurs in the intermediate slip rate range ( $0.0003 \leq V \leq 0.1 \text{ ms}^{-1}$ ), at the highest frictional work, and is associated to diffuse deformation and slip strengthening behavior. Instead, the lowest production of amorphous nanoparticles occurs at co-seismic slip rates ( $V \geq 1.3 \text{ ms}^{-1}$ ), at the highest frictional power and is associated with strain and heat localization and slip weakening behavior. Our findings suggest that, independently of the amount of smectite nanoparticles, they produce fault weakening only when typical co-seismic slip rates ( $>0.1 \text{ ms}^{-1}$ ) are achieved. This implies that estimates of the fracture surface energy dissipated during earthquakes in natural faults might be extremely difficult to constrain.

© 2017 Elsevier B.V. All rights reserved.

## 1. Introduction

Amorphous and crystalline nanoparticles are common constituents of the shallow sections of natural faults (Chester et al., 2005; Ma et al., 2006). As a consequence, a general issue in fault mechanics is how nanoparticles form and what role they have in the seismic cycle (Sammis and Ben-Zion, 2008). For instance, the

presence of nanoparticles can favor the activation of grain size-dependent deformation processes (De Paola et al., 2015) and enhance the reaction kinetics at both seismic and sub-seismic slip rates (Hirono et al., 2013). Moreover, the reduction in grain size of fault materials during seismic rupture propagation and slip affects the earthquake energy budget (Chester et al., 2005; Ma et al., 2006; Reches and Dewers, 2005). Production of nanoparticles increases some energy sinks (e.g., the breakdown work or the energy dissipated during rupture propagation, Tinti et al., 2005) at the expense, for instance, of the seismic radiated energy (Kanamori and Rivera, 2006). Here, given the abundance of smectite-rich gouges in natural faults, we focus on the investigation of the deformation

\* Corresponding author at: School of Earth and Environmental Sciences, The University of Manchester, Williamson Building, Oxford Road, Manchester M13 9PL, UK.  
E-mail address: stefano.aretusini@postgrad.manchester.ac.uk (S. Aretusini).

conditions that lead to the production of nanoparticles in these materials.

Smectite minerals, i.e. hydrous aluminum phyllosilicates, are common gouge constituents in shallow fault zones, and are among the major components of fault cores sampled during the scientific drilling of several seismogenic faults (e.g., Chester et al., 2013; Holdsworth et al., 2011; Kuo et al., 2009; Ohtani et al., 2000; Schleicher et al., 2010). Detailed microstructural studies on gouge samples from scientific drilling in the Nojima fault (Janssen et al., 2013), the San Andreas fault (Janssen et al., 2010), and the Chelungpu fault (Janssen et al., 2014; Kuo et al., 2009) reported amorphous and nanocrystalline materials associated with smectite-rich fault rocks. These materials included glass, amorphous rims around quartz grains, and partly to fully amorphous nanoparticles, often associated with recrystallized smectite minerals (Janssen et al., 2013; Kuo et al., 2009; Schleicher et al., 2010). Amorphous materials and nanoparticles have also been described in exhumed fault rocks, formed at the expense of granitic (Ozawa and Takizawa, 2007) and graphite-rich gouges (Nakamura et al., 2015). In general, understanding the processes and conditions that lead to nanoparticles and amorphous materials production in fault rocks, will help to interpret the chemical and physical processes active during the seismic cycle at shallow depths.

The production of nanoparticles can occur by cataclasis, wear, and mechanical solid state amorphization, which can reduce initial grain size down to less than 100 nm and introduce lattice defects in the crystalline solids (e.g., Hadizadeh et al., 2015; Yund et al., 1990). During and immediately after seismic slip the temperature increase in the slipping zone due to frictional heating enhances diffusional processes and may facilitate recovery of lattice defects and decrease the degree of amorphization (De Castro and Mitchell, 2002).

The effect of nanoparticles on bulk friction has been explored mainly for granitoid and carbonatic rocks and gouges (De Paola et al., 2015; Green et al., 2015). The extremely small size and high specific surface area of nanoparticles may promote grain-size dependent deformation processes (i.e. superplastic behavior (Ashby and Verrall, 1973)), resulting in fault weakening at seismic slip rates ( $\sim 1$  m/s) and rate-weakening behavior at sub-seismic slip rates (Verberne et al., 2014). However, the processes of nanoparticle production and its effect on bulk friction at seismic slip rates in clay-rich gouges have yet to be systematically studied (Remitti et al., 2015).

Here we quantify the production of nanoparticles in smectite-bearing gouges and their effect on friction by combining rotary shear experiments with a systematic mineralogical and microstructural characterization of the experimental products. Using this information, we discuss the processes leading to the production of nanoparticles and how they influence energy partitioning and dynamic weakening during seismic slip ( $0.0003$ – $1.5$  ms $^{-1}$ ). Our conclusions apply to seismic, clay-rich faults at shallow crustal depth.

## 2. Methods

### 2.1. Starting material

Since variable proportions of smectite and quartz occur in fault cores of plate boundary faults (e.g. Kameda et al., 2015), we used four different compositions to control the effect of smectite content on nanoparticles production. We tested four materials including (i) STx-1b source clay with 60 wt.% Ca-Montmorillonite (Ca-mnt), 20 wt.% opal-CT (opal) and 20 wt.% amorphous material, purchased from Clay Minerals Society (see Section 3.2 and Table 1 for their mineral composition) (Chiperia and Bish, 2001), (ii) pure crystalline quartz powder, commercially known as “micronized quartz”, (iii) 80:20 weight proportions of STx-1b and micronized quartz to obtain 50 wt.% Ca-mnt-rich gouges, and (iv) 40:60 weight

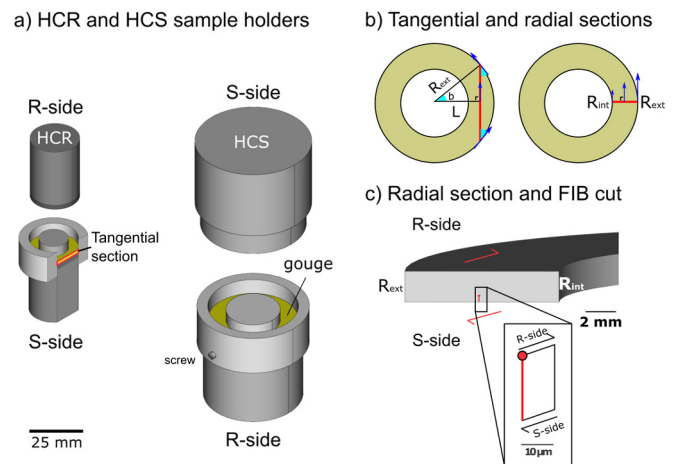


**Fig. 1.** a) The sample assemblage of the experiments performed with ROSA (HCR) and SHIVA (HCS) comprised two hollow stainless steel specimen holders (medium gray) with, respectively, 7.5/12.5 and 15/25 mm inner/outer radii ( $R_{int}/R_{ext}$ ). To confine the gouge (yellow) two Teflon parts (light grey) were used: a cylinder inserted in the inner hole and a ring positioned externally. The outer ring was cut at  $\sim 60^\circ$  to its basal surface and tightened to the metal gouge holders with a stainless steel hose clamp. In the SHIVA experiments the Teflon components were fixed with screws to the specimen metal holder. The red cross-sections represent the tangential section on HCR. b) Tangential and radial sections geometry. The tangential section is cut at a distance from the axis  $L = 0.5 \cdot (R_{int} + R_{ext})$ . Because of this, from the center to the edge of the section, radius  $r$  varies as  $R_{ext} \leq r \leq L$  and  $b$ , the angle between the section and the slip vector (blue arrows), varies as  $0^\circ \leq b \leq 37^\circ$  (according to  $b = \arccos(L/R_{ext})$ ). In the radial section geometry, radius  $r$  varies as  $R_{int} \leq r \leq R_{ext}$  and angle  $b$  is always  $90^\circ$ . c) Orientation of the FIB cut. The FIB cut is orthogonal to the radial section, therefore is parallel to the slip vector, with shear sense as indicated. (For interpretation of the references to color in this figure legend, the reader is referred to the web version of this article.)

proportions of STx-1b and micronized quartz to obtain 25 wt.% Ca-mnt-rich gouges. Before each experiment, the starting materials were equilibrated at room humidity conditions (20–45% relative humidity).

Scanning electron microscope (SEM) investigations conducted on 60 wt.% Ca-mnt revealed that the gouge had a granular appearance (grain size  $< 100$   $\mu$ m, Supplementary Fig. 1). The individual grains consisted of micrometer-sized Ca-mnt with a fibrous-like appearance, encompassing opal grains (grain size  $< 5$   $\mu$ m). Because of their intimate association, we could not separate Ca-mnt grains from opal grains. The micronized quartz powder was made of angular quartz grains (grain size  $< 100$   $\mu$ m).

### 2.2. Rotary shear experiments

Rotary shear apparatuses are currently the only experimental equipment imposing deformation conditions at seismic slip rates ( $0.0001 \leq V \leq 10$  ms $^{-1}$ ) for displacements ( $> 0.3$  m) typical of moderate to large earthquakes. To control the reproducibility of experiments we used two rotary shear apparatuses: ROSA (Rotary Shear Apparatus, model MIS-233-1-77 from MARUI & CO., LTD (Rempe et al., 2014)), installed at the University of Padova (Padua, Italy) and SHIVA (Slow to High Velocity Apparatus (Di Toro et al., 2010)), installed at the Istituto Nazionale di Geofisica e Vulcanologia (Rome, Italy). The sample assemblages for both rotary apparatuses are described in Fig. 1a.

The gouges were sheared for 3 m of equivalent displacement under a normal stress of 5 MPa (for definition of equivalent displacement, velocity, etc. see Di Toro et al., 2010). Hereafter, equivalent velocity and equivalent displacement will be referred to as slip rate and displacement, respectively. In ROSA, experiments with 60, 50 and 25 wt.% Ca-mnt were performed at slip rates of 0.0003, 0.001, 0.01, 0.1, 0.3, 1.3, 1.5 ms $^{-1}$ , while experiments with pure quartz powders were performed at slip rates of 0.01, 0.1, 1.3 ms $^{-1}$ .

**Table 1**

Resume of the Rietveld quantitative phase analysis.

Exp. (#)	V (ms <sup>-1</sup> )	Ca-mnt (wt.%)	Err. (± wt.%)	Opal-CT (wt.%)	Err. (± wt.%)	Qtz (wt.%)	Err. (± wt.%)	Amorph. (wt.%)	Err. (± wt.%)	Acc. (± wt.%)
<b>60 wt% Ca-mnt</b>										
S.M.	–	60.8	0.3	17.3	0.3	0.7	0.1	21.2	0.6	6.7
218	0.0003	38.9	0.5	16.9	0.5	0.4	0.1	43.7	1.1	6.7
210	0.001	38.2	0.5	16.3	0.5	0.6	0.1	44.9	1.0	6.7
274	0.01	41.3	0.5	17.8	0.5	0.5	0.1	40.5	1.1	6.7
216	0.1	41.3	0.5	17.1	0.5	0.6	0.0	41.1	1.0	6.7
217	0.3	50.1	0.5	18.0	0.4	0.5	0.1	31.5	0.9	6.7
238	1.5	52.0	0.5	15.5	0.5	0.4	0.1	32.1	1.0	6.7
<b>50 wt% Ca-mnt</b>										
S.M.	–	49.7	0.4	12.8	0.3	29.0	0.3	8.6	1.0	9.2
280	0.0003	30.1	0.5	10.0	0.2	29.5	0.3	30.4	1.0	9.2
245	0.001	24.7	0.6	10.9	0.3	28.4	0.3	36.1	1.2	9.2
243	0.01	28.6	0.6	11.0	0.3	32.1	0.4	28.3	1.2	9.2
229	0.1	27.1	0.5	11.6	0.3	30.2	0.3	31.1	1.1	9.2
242	0.3	36.4	0.5	11.3	0.3	27.2	0.3	25.1	1.0	9.2
228	1.5	41.2	0.6	11.1	0.3	31.5	0.4	16.3	1.2	9.2
<b>25 wt% Ca-mnt</b>										
S.M.	–	31.4	0.5	7.9	0.3	63.4	0.4	–2.7	1.3	10.1
279	0.0003	20.2	0.7	5.7	0.3	60.4	0.5	13.6	1.5	10.1
281	0.001	20.4	0.6	6.8	0.3	59.5	0.5	13.4	1.4	10.1
266	0.01	25.2	0.6	6.8	0.3	62.6	0.5	5.4	1.4	10.1
276	0.1	26.5	0.6	7.9	0.3	60.7	0.4	4.9	1.3	10.1
271	0.3	29.3	0.6	6.9	0.4	63.8	0.5	–0.1	1.5	10.1
268	1.5	27.6	0.6	6.5	0.3	61.2	0.4	4.7	1.3	10.1

Results of the quantitative XRPD phase analysis. Exp = number of the experiment; V (ms<sup>-1</sup>) = slip rate; Ca-mnt, Opal-CT, Qtz (wt.%) = Ca-Montmorillonite, Opal-CT and Quartz with err. (wt.%) = error of Rietveld refinement technique; Amorph. (wt.%) = amorphous material content and err. (wt.%) = sum of the errors for each phase; Acc. (wt.%) = accuracy of amorphous material content estimation (Section 3.2).

In SHIVA, all experiments were performed at slip rates of 0.01, 0.1 and 1.3 ms<sup>-1</sup> (see Supplementary Table 1 for a list of all the experiments and run conditions). In all experiments, the gouge layer thickness  $w$  was determined as  $w = |z - z_0|$ , with  $z_0$  the axial position measured with no gouge in the sample holder and  $z$  the axial position during the experiment. The initial gouge layer thickness  $w_0$  was measured after compacting the gouge layer at 5 MPa normal stress, before the onset of shear. All experiments had an initial gouge layer thickness  $w_0 = 2 \pm 0.15$  mm prior to deformation. The thickness  $w$  during the experiment was divided by  $w_0$  (normalized thickness =  $w/w_0$ ) to compare axial shortening data from experiments with slightly different initial thickness (Figs. 2d–f). The ratio of measured shear and normal stresses is defined as the friction coefficient  $\mu$ . The spurious friction contribution due to the sample assemblage to the total measured friction coefficient and the differences in the mechanical data between ROSA and SHIVA experiments are discussed in Supplementary Material 3.

### 2.3. X-ray powder diffraction quantitative phase analyses

X-ray powder diffraction (XRPD) with internal standard measurement and subsequent Rietveld refinement of the diffractograms allowed us to quantify the effect of shear deformation on the mineral assemblage and on the amount of amorphous material. XRPD data were collected for 25, 50, 60 wt.% Ca-mnt, on both the starting and deformed materials retrieved from the experiments performed with ROSA (Table 1). We analyzed the entire gouge layer to avoid compositional variability due to incomplete sampling. Before each measurement, ca. 10 wt.% of alumina internal standard (NIST 676A) was added to the samples.

Data were collected with a  $\theta/\theta$  diffractometer (PANalytical X'Pert Pro) equipped with a fast, real time multiple step detector, and CuK $\alpha$  radiation (40 kV and 40 mA). To secure a random smectite orientation and thus avoid grain orientation bias, sample powders were mounted on a silica glass holder using the side loading technique. We used the following instrumental conditions: 3–80°  $2\theta$  range, virtual step scan of 0.0167°  $2\theta$ , and virtual time

per step of 50 s. The incident beam pathway included: 0.125° divergence slit, 0.125° anti-scattering slit, 0.02 rad soller slits, and a 10-mm copper mask. The pathway of the diffracted beam included a Ni filter, soller slits (0.02 rad), and an antiscatter blade (5 mm).

Quantitative phase analysis (i.e., determination of both crystalline and amorphous weight content) was performed using the combined Rietveld and refined intensity ratio methods (Gualtieri, 2000). Rietveld data analysis was performed using the Profex-BGMN software (Bergmann et al., 1998), which allowed us to simulate the contribution of the instrument to the broadening of the Bragg's peaks and to implement complex structural models required by smectite and opal-CT mineralogy (i.e. smectite turbostratic disorder and opal cristobalite–tridymite interlayering). Structural models of the minerals recognized in the gouge were taken from the BGMN library for quartz and for the alumina internal standard (NIST 676a) (Bergmann et al., 1998). For Ca-mnt, we used the structural model comprising the turbostratic disorder (Ufer et al., 2009), and for opal-CT we used a supercell model simulating the irregular cristobalite–tridymite interlayering (R. Kleeberg, personal communication). Refinement was limited to the 12–60°  $2\theta$  interval to exclude the 001 peak of Ca-mnt from the refinement. The Ca-mnt 001 peak intensity is sensitive to preferred orientation, and peak position to the relative humidity in the measuring chamber. In general, the use of models accounting for Ca-mnt turbostratic disorder and opal-CT interlayered structure strongly improved the accuracy of the refinement.

### 2.4. Microstructural analysis

Techniques as scanning electron (SEM) and transmission electron microscopy (TEM) were necessary to observe deformed materials microstructures in a wide range of magnifications, down to the nanometer scale. Starting material and deformed gouge layers were (i) embedded within epoxy resin (Araldite2020®, Epofix), (ii) cut perpendicular to the slip surface (radial or tangential sections, Fig. 1b), and (iii) polished in dry conditions for SEM investigations. Twenty-four gouge layers (ROSA experiments) were cut

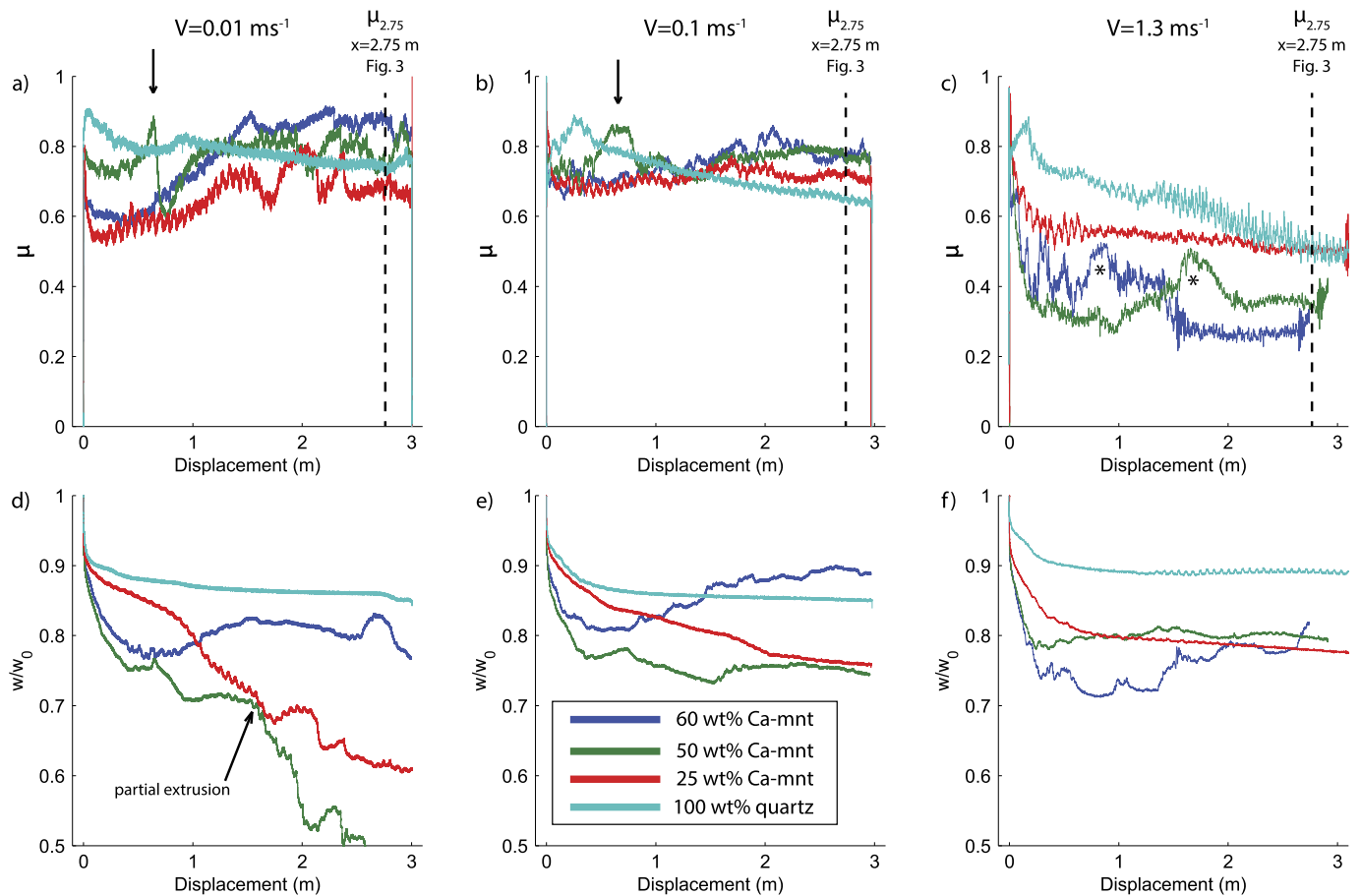


**Fig. 2.** Friction coefficient  $\mu$  (a to c) and normalized thickness  $w/w_0$  (d to f) versus displacement for experiments performed at  $V = 0.01, 0.1$  and  $1.3 \text{ ms}^{-1}$  in ROSA. The black dashed lines mark the position for the averaged value  $\mu_{2.75}$  (see Fig. 3, Supplementary Table 1). Black arrows in a) and b) mark the second peak in friction coefficient observed in 50 wt.% Ca-mnt experiments at  $V \leq 0.1 \text{ ms}^{-1}$ ; the arrow in d) marks the onset of gouge extrusion for 25 and 50 wt.% Ca-mnt experiments at  $V = 0.01 \text{ ms}^{-1}$ . Stars in c) mark large variations in friction coefficient (60 and 50 wt.% Ca-mnt experiments at  $1.3 \text{ ms}^{-1}$ ).

and polished along a tangential section (Figs. 1a–b). The polished blocks were investigated using backscattered electron (BSE) imaging within a CamScan MX3000 SEM (University of Padova). With SEM microscopy, deformed textures were imaged at low magnifications only, as sub-micrometric particles could not be analyzed.

To perform high magnification imaging, assess crystalline or amorphous nature by electron diffraction and measure composition of deformed materials, four additional samples were prepared for TEM analysis. Samples with 60 wt.% Ca-mnt (starting and sheared materials at  $V = 0.01, 0.1$ , and  $1.5 \text{ ms}^{-1}$ ) deformed with SHIVA were cut and polished along a radial section (Fig. 1b). Ultrathin, electron-transparent lamellae (100–150 nm thick, oriented as in Fig. 1c), were prepared using a FEI Helios Nanolab FIB–SEM (Utrecht University). FIB–SEM sample preparation prevented the disruption of microstructures before the TEM analysis. The FIB–SEM lamellae were analyzed in FEI Tecnai 20 F and FEI Talos F200X transmission electron microscopes (TEM) operating at 200 kV (Utrecht University), using bright field (BF) and high-angle annular dark-field (HAADF) imaging as well as selected area electron diffraction (SAED) and energy dispersive X-ray spectroscopy (EDS).

### 3. Results

#### 3.1. Rotary shear experiments

##### 3.1.1. Evolution of the friction coefficient with displacement

We obtained reproducible mechanical data using ROSA and SHIVA at identical imposed deformation conditions (see Sup-

plementary Material 2). Experiments performed at slip rates of  $0.0003\text{--}0.01 \text{ ms}^{-1}$  resulted in similar mechanical data (Fig. 2a). Friction coefficient,  $\mu$ , in pure quartz gouges decreased with displacement (slip-weakening behavior), whereas  $\mu$  in Ca-mnt bearing gouges increased with displacement (slip-strengthening behavior), after a short weakening phase in the first  $\sim 0.1 \text{ m}$  of slip (Fig. 2a). A second peak of friction and a subsequent, reproducible, friction drop occurred after ca.  $0.75 \text{ m}$  of displacement on 50 wt.% Ca-mnt gouges (arrow in Fig. 2a; Supplementary Material 2).

Experiments performed at slip rates of  $0.1\text{--}0.3 \text{ ms}^{-1}$  resulted in similar mechanical data (Fig. 2b). Pure quartz gouge was slip-strengthening in the first  $\sim 0.4 \text{ m}$  of displacement, after which it attained a monotonic slip-weakening behavior. In contrast, gouges with Ca-mnt had an initial peak friction coefficient followed by slip-weakening and, after ca.  $0.1 \text{ m}$  of displacement, by slow and monotonic slip-strengthening until slip ceased. In general, slip-strengthening was less pronounced compared to the experiments performed at  $0.0003 \leq V \leq 0.01 \text{ ms}^{-1}$ . The 50 wt.% Ca-mnt gouge had a second peak in  $\mu$  after  $\sim 1 \text{ m}$  of displacement and a subsequent drop in friction (arrow in Fig. 2b).

Experiments performed at slip rates of  $1.3\text{--}1.5 \text{ ms}^{-1}$  were characterized by an approximately exponential decay of  $\mu$  with increasing displacement, consistent with results from experiments performed by Mizoguchi et al. (2007). Similar to the experiments performed at lower slip rates, quartz gouges had a short ( $<0.3 \text{ m}$ ) slip-strengthening behavior before  $\mu$  decreased monotonically with displacement (Fig. 2c). In contrast, all Ca-mnt-bearing gouges had a similar initial rapid decay of  $\mu$  towards a



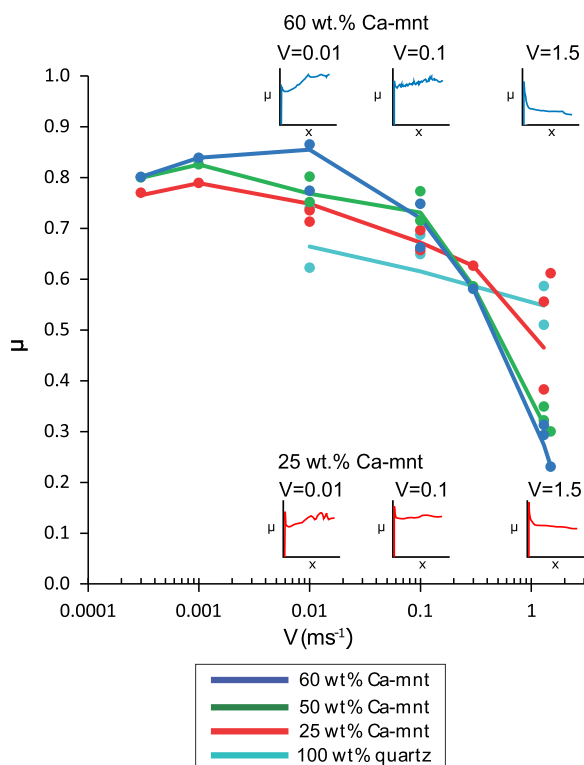


**Fig. 3.** Friction coefficient averaged between 2.725–2.775 m displacement ( $\mu_{2.75}$ ) versus slip rate. Colored lines interpolate  $\mu_{2.75}$  at increasing slip rate for different Ca-mnt content. Insets report for reference the evolution of  $\mu$  with displacement for 60 wt.% (blue line) and 25 wt.% (red line) Ca-mnt. (For interpretation of the references to color in this figure legend, the reader is referred to the web version of this article.)

minimum that decreased with increasing Ca-mnt content (Fig. 2c). For 50 and 60 wt.% Ca-mnt, after an initial monotonic slip weakening, the frictional behavior was irregular, with the occurrence of a second peak in friction between 1 and 2 m of displacement (stars in Fig. 2c).

### 3.1.2. Evolution of gouge thickness with displacement

Pure quartz gouges compacted at all imposed slip rates. In particular, large compaction at the onset of displacement was concomitant with slip-strengthening and followed by reduced to negligible compaction associated to monotonic slip-weakening until the end of the experiment (Figs. 2d–f). For all Ca-mnt gouge mixtures and independently of the imposed slip rate, compaction was concomitant with slip-weakening at the onset of displacement. With increasing slip and at all slip rates, initial compaction was followed by pronounced dilatancy for 60 wt.% Ca-mnt gouge mixtures, negligible dilatancy for 50 wt.% Ca-mnt mixtures and further compaction for 25 wt.% Ca-mnt mixtures (Figs. 2d–f). In our experiments, extrusion of powders from the sample holder occurred in the 25 and 50 wt.% Ca-mnt mixtures sheared at  $V = 0.01 \text{ ms}^{-1}$  for displacements larger than ca. 1.5 m (large  $w/w_0$  decrease indicated by the arrow in Fig. 2d).

### 3.1.3. Evolution of friction coefficient with slip rate

To compare the friction coefficient values of all experiments, we calculated  $\mu_{2.75}$  as the averaged friction coefficient at  $2.75 \pm 0.025 \text{ m}$  of displacement (Fig. 3, Supplementary Table 1). Any variation of  $\mu_{2.75}$  with slip rate is described here as either rate-weakening (friction coefficient decreases with slip rate) or rate-strengthening (friction coefficient increases with slip rate). In pure quartz gouges,  $\mu_{2.75}$  was rate-weakening. Instead, in Ca-mnt gouges  $\mu_{2.75}$  evolved from rate-strengthening to rate-weakening

with increasing slip rate. The slip rate at which the frictional behavior changed was composition-dependent:  $V = 0.01 \text{ ms}^{-1}$  in 60 wt.% and  $V = 0.001 \text{ ms}^{-1}$  in 50 and 25 wt.% Ca-mnt.

### 3.2. Quantitative phase analysis and the amount of amorphous material

The accuracy of the estimation of amorphous material content depended on: (i) the actual amount of amorphous material, (ii) the amount of internal standard added prior to the XRPD measurements, and (iii) the error of Rietveld refinement model (Westphal et al., 2009). In this study, the actual amount of amorphous material varied between  $\pm 6.7$  to  $\pm 10.1 \text{ wt.}\%$  with respect to the estimated content (Table 1, error bars in Fig. 4). Such variation was calculated considering: (i) 10 wt.% of internal standard, (ii) 1% of Rietveld error, and (iii) actual amount of amorphous material of 25, 10 and 5 wt.% (for 60, 50 and 25 wt.% Ca-mnt, respectively).

The weight fraction of the amorphous material (Section 2.3) increased with respect to its initial concentration in all the sheared Ca-mnt gouges. However, for the gouge with a 25 wt.% Ca-mnt mixtures, zero or negative values represent amorphous content close to the detection limit (Fig. 4, Table 1). The increase of amorphous material was associated with the decrease of Ca-mnt abundance and was higher in the experiments performed at low slip rates. Instead, the opal and quartz content was the same in both the starting material and all the experiments. The quantitative phase analysis suggests that the production of amorphous material occurred at the expense of Ca-mnt at all slip rates and that it was more efficient at  $V \leq 0.1 \text{ ms}^{-1}$ .

### 3.3. Microstructures

Following previous investigations conducted on clay-rich gouges deformed with rotary shear machines (French et al., 2014; Kitajima et al., 2010), we described microstructures by defining four types of microstructural domains, distinguished by grain size and by the presence of clay-clast aggregates (CCAs) (Boutareaud et al., 2008; Ferri et al., 2011) and micro-foliations (Figs. 5–6). The occurrence of the four domains in the deformed gouges as a function of the initial Ca-mnt content and of the imposed slip rate is presented in Figs. 7–8.

**Domain U (Undeformed)** has angular quartz clasts and sub-rounded aggregates of opal and Ca-mnt, with relative abundances dependent on the starting composition (Fig. 5a). At the nano-scale, the Ca-mnt is interlayered with opal (Figs. 6a–b). SAED of Ca-mnt crystals reveal a pattern with diffraction rings, suggestive of a partially crystalline to fully crystalline structure (Fig. 6a). Domain U is identical to the undeformed starting material (Supplementary Fig. 1).

**Domain LS (Low Strain)** has sub-rounded opal and quartz clasts, with grain size smaller than in domain U. In gouges with Ca-mnt  $\geq 50 \text{ wt.}\%$ , clasts are surrounded by a Ca-mnt-rich matrix and form CCAs with Ca-mnt cortex surrounding opal or quartz nuclei (Fig. 5b). In gouges with 25 wt.% Ca-mnt, CCAs are absent and the matrix is enriched in quartz.

**Domain HSf (High Strain foliated)** is organized in two subdomains: A and B (Fig. 5c). Both subdomains include individual nanoparticles, nanoparticles clusters, nanocrystals, and CCAs with opal or quartz core and a nanoparticle cortex (Figs. 6c–e). Subdomain A has a foliated texture, sub-micrometric grain size, and few CCAs. Subdomain B has a granular texture with abundant CCAs. The widespread presence of CCAs in B suggests lower shear strain compared to A (see Rempe et al., 2014 for discussion). In subdomains A and B, SAED patterns show both diffuse scattering and diffraction rings, due to the coexistence of amorphous nanoparticles and Ca-mnt nanocrystals (subset in Fig. 6d). Based on EDS-TEM element mapping, nanoparticles contain Al and Si suggesting a smectitic composition (Fig. 6f).

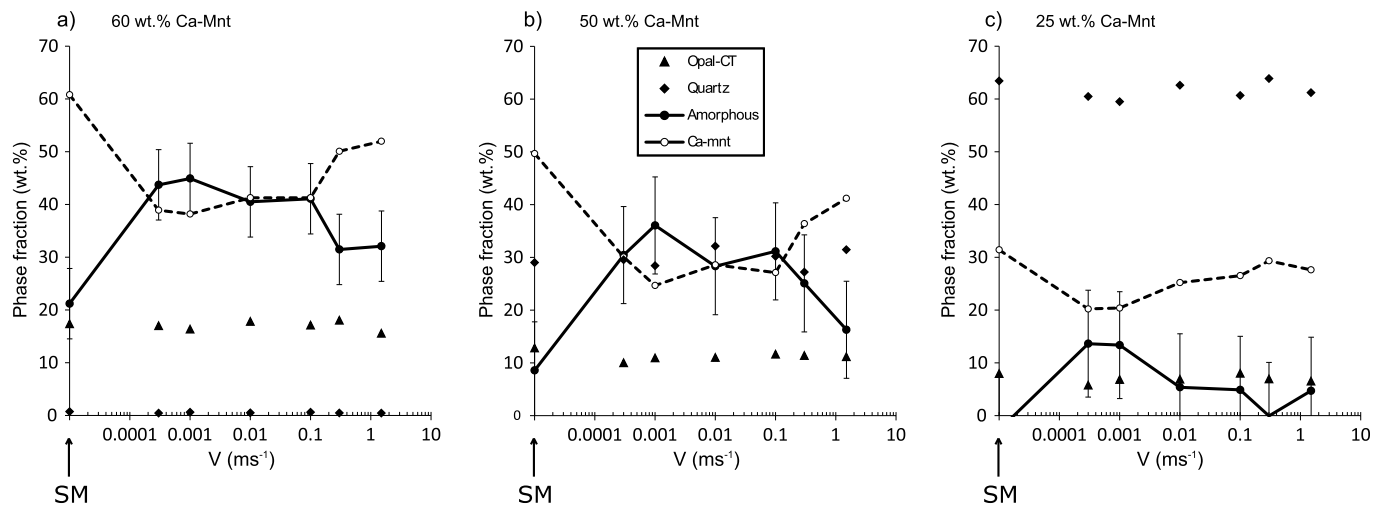


**Fig. 4.** Quantitative phase analysis results (Section 3.2 and Table 1). Phase content is plotted versus slip rate (arrows indicate the undeformed materials), for each composition: a), b) and c) for 60, 50 and 25 wt.% Ca-mnt, respectively. Error bars show the accuracy of the amorphous phase estimate calculated after (Westphal et al., 2009) (Section 2.3, Table 1). Opal and quartz wt.% are independent of the imposed slip rate. Instead, for all tested initial gouge mixtures, the amount of amorphous material increases at the expense of Ca-mnt with decreasing slip rate.

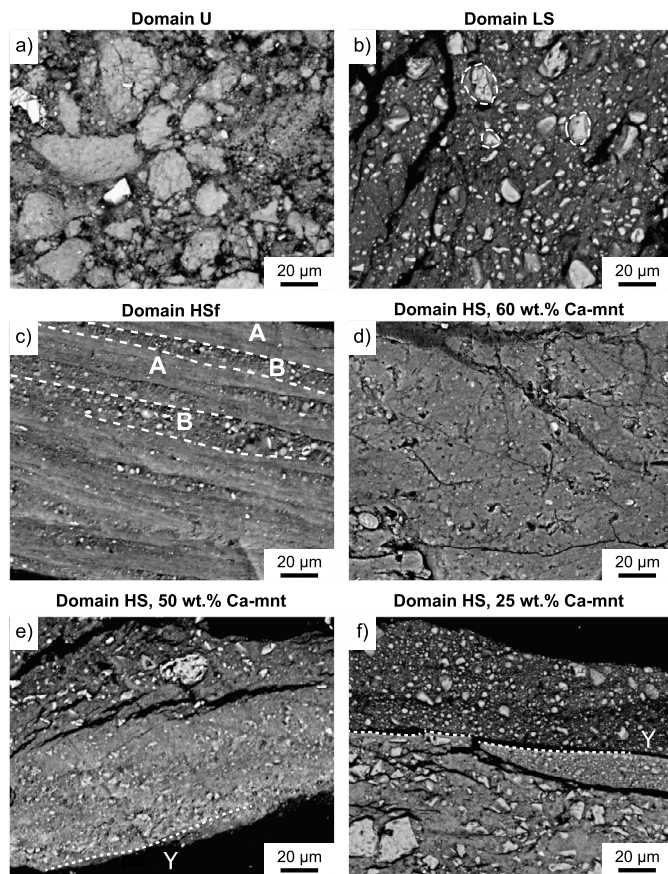


**Fig. 5.** Backscattered SEM images of the microstructural domains. a) Domain U (60 wt.% Ca-Mnt) contains angular quartz clasts and sub-rounded aggregates of opal and Ca-mnt (grain size <100 µm); b) domain LS (60 wt.% Ca-Mnt), characterized by sub-rounded opal and quartz clasts (grain size <20–50 µm). Clasts form CCAs and are surrounded by a Ca-mnt-rich matrix; c) domain Hsf (60 wt.% Ca-Mnt), with dashed lines delimiting subdomains A and B. A has a foliated, sub-micrometric texture. B has abundant CCAs (<2 µm) in a sub-micrometric matrix. d) Domain HS (60 wt.% Ca-mnt) has a sub-micrometric texture, similar to A, but with no foliation. e) Domain HS (50 wt.% Ca-mnt) is similar to d), despite a higher abundance of quartz in the sub-micrometric matrix and occurrence of occasional wavy Y-shears (white dashed line). f) Domain HS (25 wt.% Ca-mnt) has abundant sub-rounded quartz and opal grains (0.1–5 µm) in a Ca-mnt matrix, crosscut or delimited by wavy Y-shears (white dashed line).

**Domain HS (High Strain)** is similar to subdomain Hsf-A (i.e., presence of nanoparticles, Ca-mnt crystals and CCAs), but is not foliated (Figs. 5d and 6g–h). Ca-mnt crystals have periodic lattice spacing and are ubiquitous (Fig. 6h). With increasing initial quartz content (>40% in wt.), the domain HS is enriched in micrometric, sub-rounded quartz grains and is systematically cut or bounded by Y-shears (e.g., Logan et al., 1992) (Figs. 5e–f).

In general, independently of the initial gouge composition and of the imposed slip rate, high strain domains (HSf, HS) sharply crosscut the low strain (LS) or undeformed (U) domains (Fig. 7). The association of domain LS with HSf was found in gouges sheared at the lowest slip rates, which were also the gouges that recorded diffuse deformation (Fig. 7) and the largest production of amorphous material (i.e. amorphous material measured after the experiment minus amorphous material in the starting material, Fig. 8). Instead, the association of domains U or LS with HS was found in the gouges sheared at seismic slip rates, which were also the gouges that recorded localized deformation, represented by Y-shears in HS (Fig. 7), and the lowest amorphous production (Fig. 8).

## 4. Discussion

### 4.1. The amorphous nature of smectite nanoparticles

The XRPD quantitative phase analysis of the sheared gouges shows that, comparing deformed gouges (independently of the imposed slip rate) with the starting material, the amorphous material content increases and Ca-mnt content decreases, while the quantities of all the other phases remain constant (Fig. 4, Section 3.2). Consequently, Ca-mnt is the source for the produced amorphous material. Additionally, amorphous material increases in the sheared gouges compared to undeformed ones, indicating a net increase in amorphous material. The production of amorphous material represents a bulk increase of lattice disorder (i.e. decreased scattering power under X-rays) of Ca-mnt grains due to the formation of lattice defects within the grains and the increase of grain boundaries due to the reduced grain size.

SEM imaging revealed that high strain domains (HS and HSf) had an average grain size below 1 µm (Figs. 5c to 5f). In gouges with 60 wt.% Ca-Mnt, TEM imaging revealed that nanoparticles were abundant in the high strain domains (Figs. 6c–d). SAED and TEM imaging demonstrated that nanoparticles were either predominantly amorphous (domain Hsf, Fig. 6d) or crystalline (do-



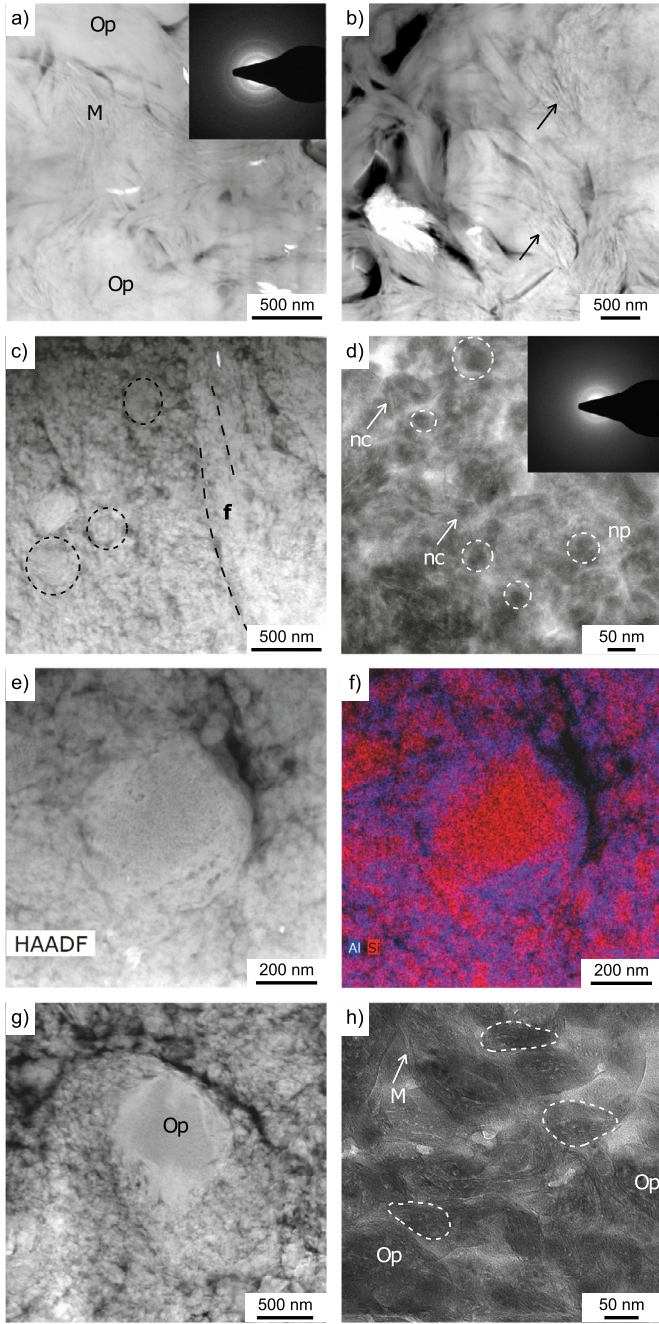


**Fig. 6.** TEM images of the microstructural domains. a) Domain U: Ca-mnt (M) and Opal (Op) (HAADF image); SAED subset shows Ca-mnt diffraction rings. b) Domain U: in some areas (black arrow), Ca-mnt and opal are interlayered (HAADF image). c) Domain HSf: rounded clusters of nanoparticles, (grain size <200 nm, black dashed circles) (HAADF image). The foliation is a fiber-shaped nanoparticle clusters ('f', black dashed lines). d) Domain HSf: nanoparticles (grain size 10–50 nm, 'np', white dashed lines) and Ca-mnt nanocrystals (grain size 5–50 nm, 'nc', white arrows) (BF image); SAED diffraction pattern showing diffuse scattering from nanoparticles and diffraction rings from nanocrystals. e) CCA within domain HSf (grain size <500 nm), having opal or quartz core and nanoparticle cortex (HAADF image); f) TEM-EDS chemical map in same area of e): the nanoparticles in the cortex have a Ca-mnt, Al-rich composition (purple). Si-rich areas (red) coincide with smaller opal (or quartz) grains. g) Domain HS: CCA (grain size ~700 nm), with opal core and nanoparticle cortex, in the nanoparticle-rich matrix (HAADF image). h) Domain HS: nanoparticles structured as nano-CCAs (white dashed contour), with opal cores rimmed by Ca-Mnt nanocrystals. Nanocrystals have a visible lattice periodicity (BF image). (For interpretation of the references to color in this figure legend, the reader is referred to the web version of this article.)

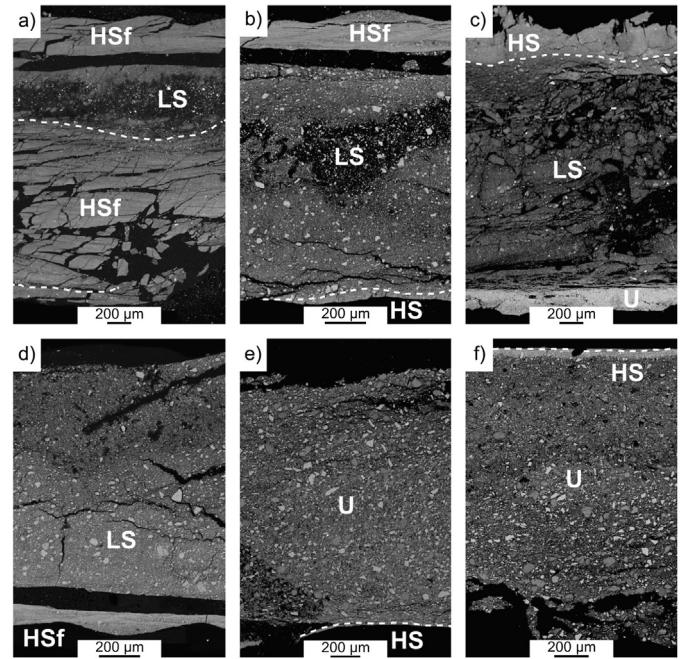


**Fig. 7.** Backscattered SEM images of the sheared gouge layers. Slipping zones from Ca-mnt  $\geq 50$  wt.% (a to c) and Ca-mnt = 25 wt.% (d to f) starting material, deformed at  $V = 0.001 \text{ ms}^{-1}$ ,  $V = 0.1 \text{ ms}^{-1}$  and  $V = 1.3 \text{ ms}^{-1}$ , respectively. The distribution of the microstructural domains is dependent on both initial composition and imposed slip rate (see Fig. 8). The white dashed lines mark the boundaries between microstructural domains.

main HS, Fig. 6h). We conclude that the amorphous material measured with XRPD in the bulk gouge is representative of the abundance of nanoparticles (both amorphous and crystalline). However, amorphous material production may be higher when associated with amorphous nanoparticles in domain HSf, due to the combination of domain thickness (Fig. 9a) and increased amorphization degree of the single nanoparticles (Fig. 6).

#### 4.2. Formation of nanoparticles and mechanical properties

In gouges with 50 and 60 wt.% Ca-mnt, the thickness of the domain HSf and thus the content of amorphous nanoparticles varies with slip rate (Fig. 9a). Amorphous nanoparticles are more abundant when associated to slip strengthening ( $V \leq 0.1 \text{ ms}^{-1}$ ). Conversely, amorphous nanoparticles are less abundant when associated to slip neutral ( $0.1 \leq V \leq 0.3 \text{ ms}^{-1}$ ) or weakening ( $V \geq 1.3 \text{ ms}^{-1}$ ) behavior (Fig. 2).

The slip strengthening behavior results in work hardening, which induces cataclasis, wear, and mechanical amorphization. Nanoparticles have a high strength as their grain size is close to the minimal size attainable by fracturing and wear processes (Sammis and Ben-Zion, 2008). If nanoparticles reach the minimum grain size by fracturing, further deformation is accommodated by plastic processes (i.e. dislocation glide at low temperatures or high slip rates), possibly leading to accumulation of lattice defects and therefore to solid-state amorphization. During deformation, if nanoparticles have high strength, shear deformation may transfer (strain delocalization) to the coarser and weaker low strain (LS) domain. During the experiment this process could lead to the thickening of the amorphous nanoparticle-rich, high strain foliated (HSf) domain and, possibly, to slip strengthening behavior.

Frictional behavior evolves from slip-neutral (for  $0.1 \leq V \leq 0.3 \text{ ms}^{-1}$ ) to slip-weakening ( $V \geq 1.3 \text{ ms}^{-1}$ ), with progressively more efficient strain localization in domain HS. In this domain, the larger abundance of crystalline nanoparticles can be related to strain and heat localization determining either a less complete

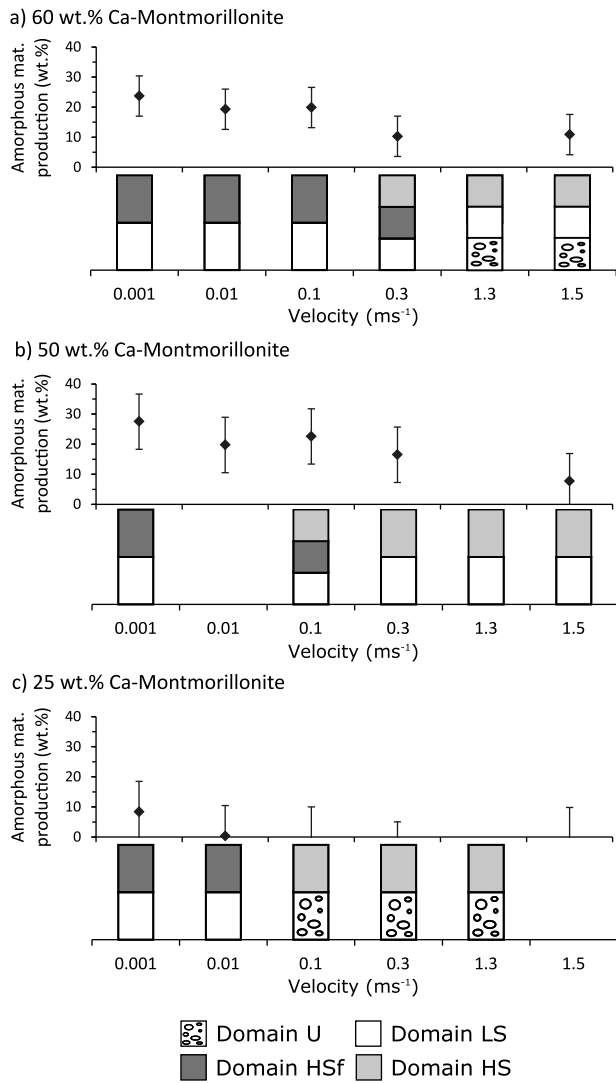


**Fig. 8.** Occurrence of the microstructural domains and amorphous material production (i.e. amorphous material after the experiment minus amorphous material in the starting material) with respect to the composition of the starting materials and slip rate. a) to c) Ca-mnt content of 60, 50 and 25 wt.% in the starting material. Domain U was found in experiments at  $V \geq 1.3 \text{ ms}^{-1}$  (60 wt.% Ca-mnt) and at  $V \geq 0.1 \text{ ms}^{-1}$  (25 wt.% Ca-mnt). Domain LS was found in all the experiments except those at  $V \geq 0.1 \text{ ms}^{-1}$  (25 wt.% Ca-mnt). Domain HSf was found in the gouges sheared at  $V \leq 0.1 \text{ ms}^{-1}$  (Ca-mnt  $\geq 50 \text{ wt.}\%$ ), and at  $V \leq 0.01 \text{ ms}^{-1}$  (25 wt.% Ca-mnt). Domain HS was found at  $V \geq 0.3 \text{ ms}^{-1}$  in 60 wt.% Ca-mnt and at  $V \geq 0.1 \text{ ms}^{-1}$  in 50 and 25 wt.% Ca-mnt gouges. The largest production of amorphous materials (25–28 wt.%) occurs for Ca-mnt  $\geq 50\%$ , low slip rates and in the presence of domain HSf.

amorphization process (i.e. because, as mechanical energy is dissipated into heat, less energy is available for amorphization) or to a more efficient recovery mechanism for lattice defects that reduces the degree of amorphization of the nanoparticles. Here, a positive feedback with strain localization may occur, with heat localization favoring grain size dependent deformation processes, reducing nanoparticles strength and favoring further strain localization. At seismic slip rates ( $V \geq 1.3 \text{ ms}^{-1}$ ), we suggest that smectite nanoparticles have a superplastic behavior which leads to frictional weakening (e.g., Green et al., 2015; Verberne et al., 2014). At the same time, we cannot exclude that part of the frictional weakening may occur as a result of Ca-mnt dehydration and consequent pore fluid (liquid or vapored water) overpressure during cataclasis and amorphization (Brantut et al., 2008; Ferri et al., 2011). However, we did not identify any fluidization

texture in domain HS that could be indicative of pore fluid pressurization.

In gouges with 25 wt.% Ca-mnt, the production of amorphous nanoparticles is limited, concomitant to slip strengthening ( $V \leq 0.001 \text{ ms}^{-1}$ ) (Fig. 9a) and associated with domain HSf (Fig. 8c). At higher slip rates, production of amorphous nanoparticles is negligible, concomitant to slip weakening and associated with domain HS. In pure quartz gouges, slip weakening occurs at all tested slip rates ( $0.01 \leq V \leq 0.3 \text{ ms}^{-1}$ ) and is associated with the formation of domain HS. In these smectite-poor cases, the formation of the HS domain is indicative of efficient strain localization compared to the smectite-rich gouges. Efficient strain localization limits the gouge volume affected by mechanical amorphization, and consequently induces a negligible production of amorphous material. Strain localization can be enhanced at  $V \geq 0.001 \text{ m/s}$  as quartz-rich gouges showed efficient dynamic weakening due to silica gel formation (Di Toro et al., 2004).

To generalize the experimental conditions at which amorphous nanoparticles are produced we introduce the frictional work density (FWD), representing the total work dissipated in the slipping zone and the frictional power density (FPD), representing the total power dissipated in the slipping zone (e.g., Di Toro et al., 2011). These can be defined as:

$$FWD = \int_0^X \tau(x) dx \quad (1)$$

with  $X$  the total displacement and  $\tau(x)$  the shear stress evolution with displacement  $x$ , and

$$FPD = FWD / \Delta t \quad (2)$$

with  $\Delta t$  the duration of the experiment (Supplementary Table 1).

In the experiments discussed here, the production of amorphous nanoparticles increased with frictional work density (Fig. 9b) and decreased with frictional power density (Fig. 9c). The relationships between the production of amorphous material and the occurrence of microstructural domain HSf (Figs. 8 and 9a), the frictional work (Fig. 9b), the frictional power (Fig. 9c) densities and slip rates (Fig. 9), suggest that the largest production of amorphous nanoparticles occurred with frictional work densities larger than  $10 \text{ MJ m}^{-1}$  and frictional power densities lower than  $0.4 \text{ MW m}^{-2}$ . These trends suggest that the processes of mechanical amorphization are less effective with higher frictional power densities and thus higher heat dissipation. This is coherent with the previous studies on the production of nanoparticles by wear and subsequent solid state amorphization in high energy ball milling. Therefore, mechanical heat dissipation can facilitate recrystallization or recovery of lattice defects (De Castro and Mitchell, 2002).

#### 4.3. Geological implications of nanoparticles production

Nanoparticles in smectite-rich fault gouges have been found in all cores of shallow fault sections when systematic nano-analysis were performed (Hirono et al., 2014; Janssen et al., 2015; Schleicher et al., 2010). In most cases, some nanoparticles were amorphous, though they could have been autogenic smectites formed in the pores of the fault gouge from alteration of silicate-bearing minerals or precipitated from percolating fluids (Schleicher et al., 2010). The experiments presented here were conducted under room-humidity conditions and under normal stress limited to 5 MPa, are representative of shallow depth and water depleted fault cores. In natural smectite-rich faults, water depleted conditions may occur as result of dehydration reactions. Smectite dehydration reactions begin almost at room temperature, at  $35^\circ\text{C}$  (Ferrage et al., 2007). Considering a temperature gradient



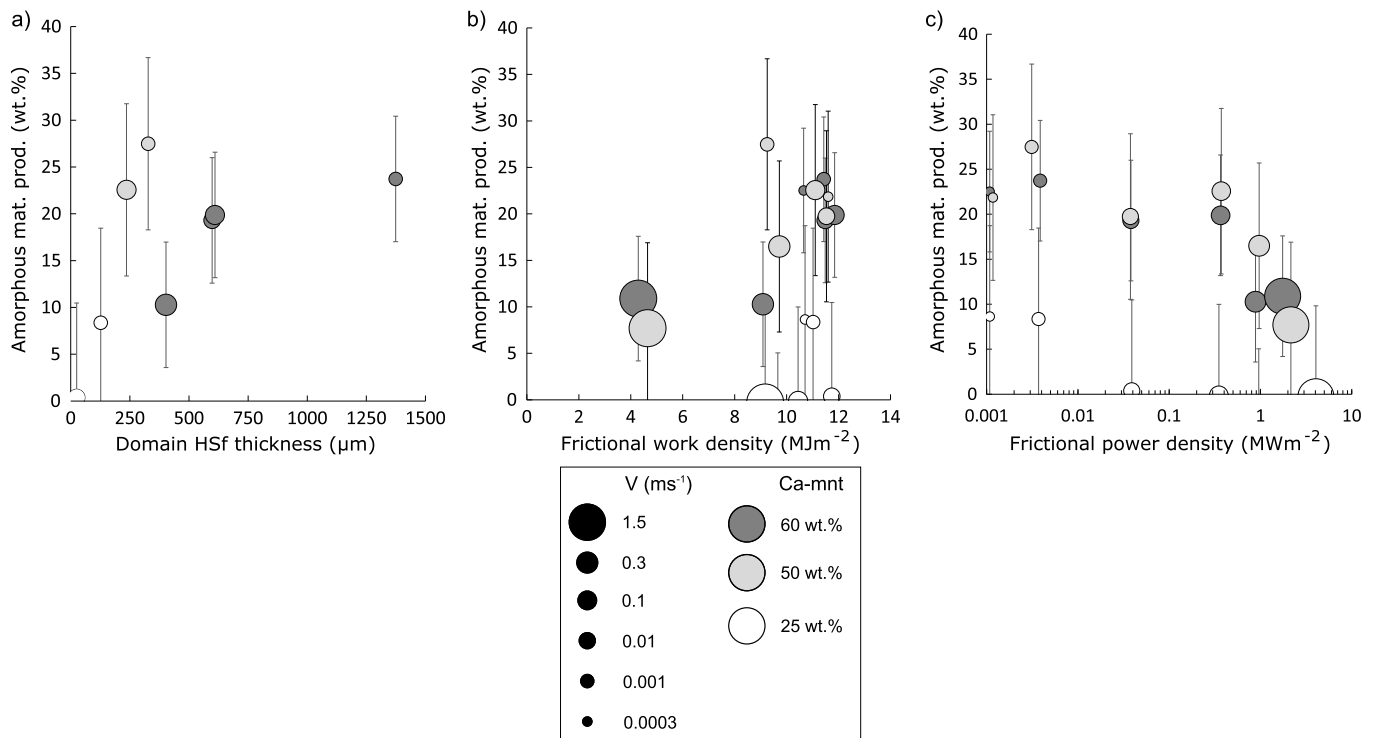


**Fig. 9.** Amorphous material production (i.e. amorphous material after the experiment minus amorphous material in the starting material) as function of domain HSf thickness, frictional work density (FWD) and frictional power density (FPD). Error bars indicate the uncertainty in the amorphous material content estimate (see also Fig. 4, Section 3.2 and Table 1). Circles size is proportional to the experiment slip rate; circles color reflects Ca-mnt content. a) Amorphous material production increases with domain HSf thickness, Ca-mnt content in the starting material and decreases with slip rate. b) Amorphous material production increases with frictional work density (FWD) independently of Ca-mnt content, especially at  $V \leq 0.1$  ms<sup>-1</sup>. c) Amorphous material production decreases with frictional power density (FPD).

of 26.3 °C km<sup>-1</sup>, as measured in Japan Trench subduction zone (Fulton et al., 2013), onset of dehydration may occur at very shallow depth (i.e. 1.3 km). Therefore, the systematic analysis of the experimental fault products presented in this work has the following implications for the mechanics of the shallow sections of smectite-rich faults.

The observed microstructure, amorphous quantification and mechanical data suggest that the production of nanoparticles is larger at high frictional work densities rather than at high frictional power densities (Fig. 9). According to Eq. (1), frictional work density increases with shear stress and, thus, with effective normal stress. As a consequence, at sub-seismic to almost seismic slip rates, nanoparticle production is expected to increase with depth, until, at higher temperatures, smectite is replaced by other minerals (e.g., illite). The frictional power density is proportional to both the effective normal stress and slip rate (Eq. (2)). Therefore, during seismic slip the amount of nanoparticle production is expected to be further reduced compared to the experiments discussed here. In fact, the slip weakening distance and the slip distance required for strain localization decreases with normal stress (Di Toro et al., 2011; Smith et al., 2015). In other words, given the same amount of slip accommodated by the fault, most nanoparticles and amorphous materials observed (and survived) in natural faults are expected to be produced during the late stages of co-seismic slip or during afterslip.

The clast size distribution in natural slipping zones has been used to estimate the breakdown work component of an earthquake energy budget (Chester et al., 2005; Ma et al., 2006). The relative abundance of nanoparticles is a major contributor to the measurement of the surface fracture energy. In the case of the Punchbowl and Chelungpu Faults, the authors used the clast size distributions to estimate that the formation of new grains dissipated up to 6% of the breakdown work during seismic faulting, the remnant being dissipated as heat on the fault plane (Chester et al., 2005;

Ma et al., 2006). However, if nanoparticles in nature were mainly produced at low slip rates, intermediate and possibly sub-seismic, as the experimental results discussed here suggest, the contribution of ultra-comminution to the breakdown work during the co-seismic slip might be overestimated or extremely difficult to constrain.

Our results also indicate that the abundance of nano-particles is not as important as the slip rate in controlling the frictional behavior of the sheared smectite-rich gouges (Figs. 2 and 4). Although smectite-rich ( $\geq 50\%$  Ca-Mnt) gouges are more velocity-weakening than smectite-poor gouges ( $< 50\%$  Ca-Mnt), the slip rate is most important in controlling the overall frictional behavior (Fig. 3). The direct extrapolation of our experimental observations to nature would imply that the formation of smectite nanoparticles may induce strengthening or weakening depending on the slip rate and, to a less extent, on the smectite content. The slip-strengthening behavior contemporary to the large production of nanoparticles at intermediate slip rates (Figs. 2 and 4) may have the following implications: at slip rates  $\sim 1$  mm/s or less (during the late stages of co-seismic slip or during afterslip); slip-strengthening will induce either the arrest of fault slip (if the fault core is stronger than the principal slipping zone) or the thickening of the principal slipping zone (if fault core is weaker than nanoparticle-rich principal slipping zone). Approaching seismic slip rates, the presence of nanoparticles produced by mechanical amorphization, which have high lattice disorder and reduced activation energy for decomposition reactions, will allow a more efficient release of OH-groups (and thermomechanical pressurization), decreasing temperatures at which dynamic weakening will occur (Hirano et al., 2013). Although thermal pressurization of pore fluids probably have a pivotal role in dynamic weakening of smectite-rich gouges (Veveakis et al., 2007), there is no reason to exclude that, especially with progressive seismic slip, thermochemical pressurization (Brantut et al., 2008; Ferri et al., 2011) and possibly grain-size

dependent processes (De Paola et al., 2015; Green et al., 2015; Spagnuolo et al., 2015; Verberne et al., 2014) may contribute to dynamic weakening of natural faults. Considering the results presented in Fig. 2, the larger is the abundance of nanoparticles the faster should be the seismic dynamic weakening in natural slip-ping zones.

## 5. Conclusions

We conducted a series of rotary shear experiments on 60–40 wt.%, 50–50 wt.%, 25–75 wt.% smectite (Ca-montmorillonite, Ca-mnt) – quartz + opal mixtures and on pure quartz gouges. All experiments were performed under room humidity conditions (20–45% relative humidity) on a 2-mm thick gouge layer by imposing the same normal stress (5 MPa) and displacement (3 m), whereas slip rates ranged from 0.0003 to 1.5 ms<sup>−1</sup> (Supplementary Table 1). We analyzed the starting and the deformed materials with SEM, FIB-SEM, TEM and XRPD quantitative phase analysis to describe the microstructures, determine the mineral content and production of amorphous material depending on the experimental conditions (Figs. 4–8). The main conclusions are:

- 1) Nanoparticles (Fig. 6), found in high strain microstructural domains (HSf and HS; Fig. 5), are produced by mechanical solid state amorphization of Ca-mnt (Fig. 4). Nanoparticles are mainly amorphous in domain HSf and crystalline in domain HS (Fig. 6).
- 2) Nanoparticles production and degree of amorphization vary with slip rate and composition depending on the degree of strain localization. The maximum production of amorphous nanoparticles (20 wt.%) occurs at intermediate slip rates ( $0.0003 \leq V \leq 0.1 \text{ ms}^{-1}$ ), high Ca-mnt abundance (Ca-mnt  $\geq 50 \text{ wt.}\%$ ), concomitant to strain delocalization in the gouge layer associated to slip-strengthening behavior. With decreasing smectite content, maximum production is limited to the lowermost slip rates (i.e. at  $0.0003 \leq V \leq 0.01 \text{ ms}^{-1}$  with 25 wt.% Ca-mnt). In contrast, the production of crystalline nanoparticles (5–10 wt.%) occurs at co-seismic slip rates ( $V \geq 1.3 \text{ ms}^{-1}$ ), concomitant to strain localization in the gouge layer associated to slip weakening behavior.
- 3) Amorphous nanoparticle production changes with slip rate depending on dissipation of mechanical energy. Maximum production of amorphous nanoparticles occurs with large frictional work (10 MJm<sup>−1</sup>) and low frictional power (0.4 MWm<sup>−2</sup>) densities.
- 4) On the basis of the experimental evidence presented here, in smectite-rich natural faults, nanoparticles are produced by cataclasis, wear and mechanical solid-state amorphization.
- 5) Several implications for natural smectite-rich faults can be made. First, fault weakening occurs only when typical seismic slip rates ( $>0.1 \text{ ms}^{-1}$ ) are achieved and the amount of weakening increases with the abundance of nanoparticles and amorphous materials. Second, since nanoparticles are more abundant when produced at intermediate and possibly sub-seismic slip rates, estimates of the fracture surface energy dissipated during earthquakes may be difficult to constrain.

## Acknowledgements

Two anonymous reviewers and the Editor are acknowledged for their very constructive comments. SA, ES and GDT acknowledge the ERC Consolidator grant 614705 NOFEAR. SA thanks Leonardo Tauro for advices on sample preparation, Federico Zorzi for help with the Rietveld modelling, Reinhard Kleeberg for the opal-CT structure used in Rietveld refinements and helpful advices on Rietveld modelling, Jacob Tielke for the help in proofreading and

improving the manuscript and Francesca Remitti for insightful discussions.

## Appendix A. Supplementary material

Supplementary material related to this article can be found online at <http://dx.doi.org/10.1016/j.epsl.2017.01.048>.

## References

- Ashby, M.F., Verrall, R.A., 1973. Diffusion-accommodated flow and superplasticity. *Acta Metall.* 21, 149–163. [http://dx.doi.org/10.1016/0001-6160\(73\)90057-6](http://dx.doi.org/10.1016/0001-6160(73)90057-6).
- Bergmann, J., Friedel, P., Kleeberg, P., 1998. BGMN – a new fundamental parameters based rietveld program for laboratory X-ray Sources, it's use in quantitative analysis and structure investigations. In: CPD Newsletter, pp. 5–8.
- Boutareaud, S., Calugaru, D.-G., Han, R., Fabbri, O., Mizoguchi, K., Tsutsumi, A., Shimamoto, T., 2008. Clay-clast aggregates: a new textural evidence for seismic fault sliding? *Geophys. Res. Lett.* 35. <http://dx.doi.org/10.1029/2007GL032554>.
- Brantut, N., Schubnel, A., Rouzaud, J.-N., Brunet, F., Shimamoto, T., 2008. High-velocity frictional properties of a clay-bearing fault gouge and implications for earthquake mechanics. *J. Geophys. Res.* 113. <http://dx.doi.org/10.1029/2007JB005551>.
- Chester, J.S., Chester, F.M., Kronenberg, A.K., 2005. Fracture surface energy of the Punchbowl fault, San Andreas system. *Nature* 437, 133–136. <http://dx.doi.org/10.1038/nature03942>.
- Chester, F.M., Rowe, C., Ujiie, K., Kirkpatrick, J., Regalla, C., Remitti, F., Moore, J.C., Toy, V., Wolfson-Schwehr, M., Bose, S., Kameda, J., Mori, J.J., Brodsky, E.E., Eguchi, N., Toczko, S., Expedition 343 and 343T Scientists, 2013. Structure and composition of the plate-boundary slip zone for the 2011 Tohoku-Oki earthquake. *Science* 342, 1208–1211. <http://dx.doi.org/10.1126/science.1243719>.
- Chiper, S.J., Bish, D.L., 2001. Baseline studies of the clay minerals society source clays: powder X-ray diffraction analyses. *Clays Clay Miner.* 49, 398–409.
- De Castro, C.L., Mitchell, B.S., 2002. Nanoparticles from mechanical attrition. In: *Synthesis, Functionalization and Surface Treatment of Nanoparticles*, pp. 1–14.
- De Paola, N., Holdsworth, R.E., Viti, C., Colletini, C., Bullock, R., 2015. Can grain size sensitive flow lubricate faults during the initial stages of earthquake propagation? *Earth Planet. Sci. Lett.* 431, 48–58. <http://dx.doi.org/10.1016/j.epsl.2015.09.002>.
- Di Toro, G., Goldsby, D.L., Tullis, T.E., 2004. Friction falls towards zero in quartz rock as slip velocity approaches seismic rates. *Nature* 427, 436–439.
- Di Toro, G., Han, R., Hirose, T., De Paola, N., Nielsen, S., Mizoguchi, K., Ferri, F., Cocco, M., Shimamoto, T., 2011. Fault lubrication during earthquakes. *Nature* 471, 494–498. <http://dx.doi.org/10.1038/nature09838>.
- Di Toro, G., Niemeijer, A., Tripoli, A., Nielsen, S., Di Felice, F., Scarlato, P., Spada, G., Alessandrini, R., Romeo, G., Di Stefano, G., Smith, S., Spagnuolo, E., Mariano, S., 2010. From field geology to earthquake simulation: a new state-of-the-art tool to investigate rock friction during the seismic cycle (SHIVA). *Rend. Lincei* 21, 95–114. <http://dx.doi.org/10.1007/s12210-010-0097-x>.
- Ferrage, E., Kirk, C.A., Cressey, G., Cuadros, J., 2007. Dehydration of Ca-montmorillonite at the crystal scale. Part 2. Mechanisms and kinetics. *Am. Mineral.* 92, 1007–1017. <http://dx.doi.org/10.2138/am.2007.2397>.
- Ferri, F., Di Toro, G., Hirose, T., Han, R., Noda, H., Shimamoto, T., Quaresimin, M., De Rossi, N., 2011. Low- to high-velocity frictional properties of the clay-rich gouges from the slipping zone of the 1963 Vajont slide, northern Italy. *J. Geophys. Res.* Solid Earth 116, 1–17. <http://dx.doi.org/10.1029/2011JB008338>.
- French, M.E., Kitajima, H., Chester, J.S., Chester, F.M., Hirose, T., 2014. Displacement and dynamic weakening processes in smectite-rich gouge from the Central Deforming Zone of the San Andreas Fault. *J. Geophys. Res.* Solid Earth 119, 1777–1802. <http://dx.doi.org/10.1002/2013JB010757>.
- Fulton, P.M., Brodsky, E.E., Kano, Y., Mori, J., Chester, F., Ishikawa, T., Harris, R.N., Lin, W., Eguchi, N., Toczko, S., 2013. Expedition 343, 343T, and KR13-08 Scientists, 2013. Low coseismic friction on the Tohoku-Oki fault determined from temperature measurements. *Science* 342, 1214–1217. <http://dx.doi.org/10.1126/science.1243641>.
- Green, H.W., Shi, F., Bozhilov, K., Xia, G., Reches, Z., 2015. Phase transformation and nanometric flow cause extreme weakening during fault slip. *Nat. Geosci.* 8, 484–489. <http://dx.doi.org/10.1038/ngeo2436>.
- Gualtieri, A.F., 2000. Accuracy of XRPD QPA using the combined Rietveld-RIR method. *J. Appl. Crystallogr.* 33, 267–278. <http://dx.doi.org/10.1107/S002188989901643X>.
- Hadizadeh, J., Tullis, T.E., White, J.C., Konkachbaev, A.I., 2015. Shear localization, velocity weakening behavior, and development of cataclastic foliation in experimental granite gouge. *J. Struct. Geol.* 71, 86–99. <http://dx.doi.org/10.1016/j.jsg.2014.10.013>.
- Hirono, T., Kameda, J., Kanda, H., Tanikawa, W., Ishikawa, T., 2014. Mineral assemblage anomalies in the slip zone of the 1999 Taiwan Chi-Chi earthquake: ultrafine particles preserved only in the latest slip zone. *Geophys. Res. Lett.* 41, 3052–3059. <http://dx.doi.org/10.1002/2014GL059805>.

- Hirono, T., Tanikawa, W., Honda, G., Kameda, J., Fukuda, J., Ishikawa, T., 2013. Importance of mechanochemical effects on fault slip behavior during earthquakes. *Geophys. Res. Lett.* 40, 2988–2992. <http://dx.doi.org/10.1002/grl.50609>.
- Holdsworth, R.E., van Diggelen, E.W.E., Spiers, C.J., de Bresser, J.H.P., Walker, R.J., Bowen, L., 2011. Fault rocks from the SAFOD core samples: implications for weakening at shallow depths along the San Andreas Fault, California. *J. Struct. Geol.* 33, 132–144. <http://dx.doi.org/10.1016/j.jsg.2010.11.010>.
- Janssen, C., Naumann, R., Morales, L., Wirth, R., Rhede, D., Dresen, G., 2015. Co-seismic and/or a-seismic microstructures of JFAST 343 core samples from the Japan Trench. *Mar. Geol.* 362, 33–42. <http://dx.doi.org/10.1016/j.margeo.2015.01.013>.
- Janssen, C., Wirth, R., Lin, A., Dresen, G., 2013. TEM microstructural analysis in a fault gouge sample of the Nojima Fault Zone, Japan. *Tectonophysics* 583, 101–104. <http://dx.doi.org/10.1016/j.tecto.2012.10.020>.
- Janssen, C., Wirth, R., Rybacki, E., Naumann, R., Kemnitz, H., Wenk, H.-R., Dresen, G., 2010. Amorphous material in SAFOD core samples (San Andreas Fault): evidence for crush-origin pseudotachylytes? *Geophys. Res. Lett.* 37, L01303. <http://dx.doi.org/10.1029/2009GL040993>.
- Janssen, C., Wirth, R., Wenk, H.-R., Morales, L., Naumann, R., Kienast, M., Song, S.-R., Dresen, G., 2014. Faulting processes in active faults – evidences from TCDP and SAFOD drill core samples. *J. Struct. Geol.* 65, 100–116. <http://dx.doi.org/10.1016/j.jsg.2014.04.004>.
- Kameda, J., Shimizu, M., Ujiie, K., Hirose, T., Ikari, M., Mori, J., Ohashi, K., Kimura, G., 2015. Pelagic smectite as an important factor in tsunamigenic slip along the Japan Trench. *Geology* 43, 155–158. <http://dx.doi.org/10.1130/G35948.1>.
- Kanamori, H., Rivera, L., 2006. Energy partitioning during an earthquake. In: Abercrombie, R., McGarr, A., Toro, G.D., Kanamori, H. (Eds.), *Earthquakes: Radiated Energy and the Physics of Faulting*. American Geophysical Union, pp. 3–13.
- Kitajima, H., Chester, J.S., Chester, F.M., Shimamoto, T., 2010. High-speed friction of disaggregated ultracataclasite in rotary shear: characterization of frictional heating, mechanical behavior, and microstructure evolution. *J. Geophys. Res.* 115. <http://dx.doi.org/10.1029/2009JB007038>.
- Kuo, L.-W., Song, S.-R., Yeh, E.-C., Chen, H.-F., 2009. Clay mineral anomalies in the fault zone of the Chelungpu Fault, Taiwan, and their implications. *Geophys. Res. Lett.* 36. <http://dx.doi.org/10.1029/2009GL039269>.
- Logan, J.M., Dengo, C.A., Higgs, N.G., Wang, Z.Z., 1992. Fabrics of experimental fault zones: their development and relationship to mechanical behavior. *Fault Mech. Transp. Prop. Rock*, 33–67. [http://dx.doi.org/10.1016/S0074-6142\(08\)62814-4](http://dx.doi.org/10.1016/S0074-6142(08)62814-4).
- Ma, K.-F., Tanaka, H., Song, S.-R., Wang, C.-Y., Hung, J.-H., Tsai, Y.-B., Mori, J., Song, Y.-F., Yeh, E.-C., Soh, W., Sone, H., Kuo, L.-W., Wu, H.-Y., 2006. Slip zone and energetics of a large earthquake from the Taiwan Chelungpu-fault Drilling Project. *Nature* 444, 473–476. <http://dx.doi.org/10.1038/nature05253>.
- Mizoguchi, K., Hirose, T., Shimamoto, T., Fukuyama, E., 2007. Reconstruction of seismic faulting by high-velocity friction experiments: an example of the 1995 Kobe earthquake. *Geophys. Res. Lett.* 34. <http://dx.doi.org/10.1029/2006GL027931>.
- Nakamura, Y., Ohashi, K., Toyoshima, T., Satish-Kumar, M., Akai, J., 2015. Strain-induced amorphization of graphite in fault zones of the Hidaka metamorphic belt, Hokkaido, Japan. *J. Struct. Geol.* 72, 142–161. <http://dx.doi.org/10.1016/j.jsg.2014.10.012>.
- Ohtani, T., Fujimoto, K., Ito, H., Tanaka, H., Tomida, N., Higuchi, T., 2000. Fault rocks and past to recent fluid characteristics from the borehole survey of the Nojima fault ruptured in the 1995 Kobe earthquake, southwest Japan. *J. Geophys. Res.* 105, 16161–16171. <http://dx.doi.org/10.1029/2000JB900086>.
- Ozawa, K., Takizawa, S., 2007. Amorphous material formed by the mechanochemical effect in natural pseudotachylyte of crushing origin: a case study of the Iida-Matsukawa Fault, Nagano Prefecture, Central Japan. *J. Struct. Geol.* 29, 1855–1869. <http://dx.doi.org/10.1016/j.jsg.2007.08.008>.
- Reches, Z., Dewers, T.A., 2005. Gouge formation by dynamic pulverization during earthquake rupture. *Earth Planet. Sci. Lett.* 235, 361–374. <http://dx.doi.org/10.1016/j.epsl.2005.04.009>.
- Remitti, F., Smith, S.A.F., Mitterperger, S., Gualtieri, A.F., Di Toro, G., 2015. Frictional properties of fault zone gouges from the J-FAST drilling project (Mw 9.0 2011 Tohoku-Oki earthquake). *Geophys. Res. Lett.* 42, 2691–2699. <http://dx.doi.org/10.1002/2015GL063507>.
- Rempe, M., Smith, S.A.F., Ferri, F., Mitchell, T.M., Di Toro, G., 2014. Clast-cortex aggregates in experimental and natural calcite-bearing fault zones. *J. Struct. Geol.* 68, 142–157. <http://dx.doi.org/10.1016/j.jsg.2014.09.007>.
- Sammis, C.G., Ben-Zion, Y., 2008. Mechanics of grain-size reduction in fault zones. *J. Geophys. Res.* 113. <http://dx.doi.org/10.1029/2006JB004892>.
- Schleicher, A.M., Van der Pluijm, B.A., Warr, L.N., 2010. Nanocoatings of clay and creep of the San Andreas fault at Parkfield, California. *Geology* 38, 667–670. <http://dx.doi.org/10.1130/G31091.1>.
- Smith, S.A.F., Nielsen, S., Di Toro, G., 2015. Strain localization and the onset of dynamic weakening in calcite fault gouge. *Earth Planet. Sci. Lett.* 413, 25–36. <http://dx.doi.org/10.1016/j.epsl.2014.12.043>.
- Spagnuolo, E., Plümpner, O., Violay, M., Cavallo, A., Di Toro, G., 2015. Fast-moving dislocations trigger flash weakening in carbonate-bearing faults during earthquakes. *Sci. Rep.* 5, 16112. <http://dx.doi.org/10.1038/srep16112>.
- Tinti, E., Spudich, P., Cocco, M., 2005. Earthquake fracture energy inferred from kinematic rupture models on extended faults. *J. Geophys. Res. Solid Earth* 110, B12303. <http://dx.doi.org/10.1029/2005JB003644>.
- Ufer, K., Roth, G., Kleeberg, R., Stanjek, H., Dohrmann, R., Bergmann, J., 2009. Description of X-ray powder pattern of turbostratically disordered layer structures with a Rietveld compatible approach. *Z. Kristallogr., Cryst. Mater.* 219, 519–527. <http://dx.doi.org/10.1524/zkri.219.9.519.44039>.
- Verberne, B.A., Plümpner, O., de Winter, D.M., Spiers, C.J., 2014. Superplastic nanofibrous slip zones control seismogenic fault friction. *Science* 346, 1342–1344. <http://dx.doi.org/10.1126/science.1259003>.
- Veveakis, E., Vardoulakis, I., Di Toro, G., 2007. Thermoporomechanics of creeping landslides: the 1963 Vaiont slide, northern Italy. *J. Geophys. Res.* 112. <http://dx.doi.org/10.1029/2006JF00702>.
- Westphal, T., Füllmann, T., Pöllmann, H., 2009. Rietveld quantification of amorphous portions with an internal standard – mathematical consequences of the experimental approach. *Powder Diff.* 24, 239–243. <http://dx.doi.org/10.1154/1.3187828>.
- Yund, R.A., Blanpied, M.L., Tullis, T.E., Weeks, J.D., 1990. Amorphous material in high strain experimental fault gouges. *J. Geophys. Res. Solid Earth* 95, 15589–15602. <http://dx.doi.org/10.1029/JB095iB10p15589>.